Journal Pre-proof

Fabrication of FeNi Hydroxides Double-shell Nanotube Arrays with Enhanced Performance for Oxygen Evolution Reaction

Nan Yu, Wei Cao, Marko Huttula, Yves Kayser, Philipp Hoenicke, Burkhard Beckhoff, Fengyu Lai, Ruohao Dong, Hongxia Sun, Baoyou Geng

Please cite this article as: Yu N, Cao W, Huttula M, Kayser Y, Hoenicke P, Beckhoff B, Lai F, Dong R, Sun H, Geng B, Fabrication of FeNi Hydroxides Double-shell Nanotube Arrays with Enhanced Performance for Oxygen Evolution Reaction, *Applied Catalysis B: Environmental* (2019), doi: https://doi.org/10.1016/j.apcatb.2019.118193

This is a PDF file of an article that has undergone enhancements after acceptance, such as the addition of a cover page and metadata, and formatting for readability, but it is not yet the definitive version of record. This version will undergo additional copyediting, typesetting and review before it is published in its final form, but we are providing this version to give early visibility of the article. Please note that, during the production process, errors may be discovered which could affect the content, and all legal disclaimers that apply to the journal pertain.

Fabrication of FeNi Hydroxides Double-shell Nanotube Arrays with Enhanced Performance for Oxygen Evolution Reaction

Nan Yu,[a] Wei Cao,[b] Marko Huttula,[b] Yves Kayser,[c] Philipp Hoenicke,[c] Burkhard Beckhoff,[c] Fengyu Lai,[a] Ruohao Dong,[a] Hongxia Sun,[a] Baoyou Geng*[a]

[a] *College of Chemistry and Materials Science, Anhui Key Laboratory of Functional Molecular Solids, Ministry of Education, The Key Laboratory of Electrochemical Clean Energy of Anhui Higher Education Institutes, Anhui Normal University, Wuhu, 241002, China.*

[b] *Nano and Molecular Systems Research Unit, University of Oulu, P.O. Box. 3000, FI-90014, Finland*

[c] *Physikalisch-Technische Bundesanstalt, X-ray Spectrometry Abbestr. 2-12, 10587 Berlin, Germany*

*E-mail: bygeng@mail.ahnu.edu.cn

Graphical Abstract

The electrocatalysts for OER based FeNi-Hydroxides nanotube arrays are successfully fabricated by in-situ reaction and Kirkendall effect. The as-synthesized tube arrays exhibit the lower overpotential and better stability for OER and overall water splitting. XANES spectra and DFT calculation reveal clearly that higher oxidation state of Fe lowers energy barrier of rate-determining step in OER.
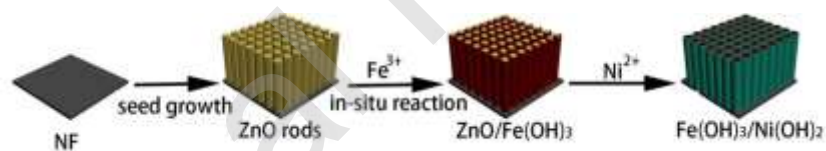
Research Highlights

- FeNi-Hydroxides nanotube arrays are successfully fabricated by in-situ reaction and Kirkendall effect.

- The as-prepared catalysts exhibit superior electrochemical performance for OER, HER and overall water splitting.

- XPS and XANES spectra show that superior performance attributes to more unoccupied Fe 3d states in FeNi-Hydroxides nanotube arrays obtained by this

synthesis method.

ABSTRCT FeNi Hydroxides (FeNi-HD) have been considered as promising substitutes to noble metal electrocatalysts for oxygen evolution reaction (OER). In this work, we design and realize FeNi-HD nanotube arrays (FeNi-HDNAs) on Ni foam via an in-situ reaction and Kirkendall effect. The obtained catalysts possess higher specific surface area, more catalytic active sites and better chemical stability for OER. Electron migrations from the Fe 3d orbitals to Ni sites in the FeNi-HDNAs lead to more unoccupied Fe 3d states and a higher oxidation state. As expected, FeNi-HDNAs exhibit lower overpotential as well as lower Tafel slope and better durability than the Fe- or Ni-HD peers. DFT calculations elucidate that FeNi hydroxides lower the energy barrier of rate-determining step in OER. Moreover, a high current density of 10 mA cm^{-2} is obtained at a low potential of 1.49 V using FeNi-HDNAs as the bifunctional electrocatalyst for overall water splitting in basic solution.

1. **Introduction**

The oxygen evolution reaction (OER) is a grand challenge in electrochemical catalysis and energy storage because of a slow 4-electron transfer reaction in kinetics [1]. Many efforts have been dedicated to developments of proper electrocatalysts to facilitate fast kinetics and routes to improve eletrocatalytic performance for OER [2-5]. Trasatti [4] concluded noble metals based electrocatalysts (IrO_2 and RuO_2) might be the most active species for OER in acidic or alkaline solutions. It was explained in density functional theory (DFT) works of Rossmeisl [6, 7], and attributed to near thermochemical equivalence of each elementary step of oxidation reaction in the catalysts.

However, the extremely scarce natural abundances of Ir and Ru impede their commercial and large-scale applications. Alternatives have been searched within earth-abundant metals and compounds with low cost, high activity and stability for OER, such as transition-metal-based catalysts (M=O, M-OH/OOH and M-B/S/Se/Te/P) [8, 9, 10] and non-metal-based components (carbon materials etc.) [11]. Among these catalysts, it is generally agreed that NiFe (oxy)hydroxides are the most promising electrocatalysts for OER because the coexistence of Ni and Fe lower overpotentials at Fe sites in water oxidation [12-16]. However, the powder catalysts are limited in application and activity enhancement due to the following disadvantages. Firstly, viscous polymer (such as Nafion) must be introduced when powder materials are processed to the electrode. This causes loss of catalytic active sites during processing and difficulty of inner particles' participations to catalytic reactions. Secondly, the powder electrocatalysts are easily exfoliated from electrode

substrate by gas bubbles of water splitting in the catalytic processes. More importantly, introduction of adhesion agent can destroy high oxidation state of Fe active sites in the electrode process. These shortages may be overcome by using conductive substrate and engineering ordered arrays structures via electrodeposition and hydrothermal method [17]. The conductive substrate can reduce the potential barrier of electrolyte-catalyst-electrode, while array structures advance on electrocatalytic process due to more catalytically active sites for reaction, more transport channels for electrolysis and hydrophobic surface for gas escape [18]. Nevertheless, most of the obtained structures remain as sheets or thin films. The sheet flakes on substrates lack active sites due to the unavailability of inner components during the OER. The super thin sheets/film can hardly disperse evenly, resulting in edge crispation and mutual coverage. Hence, novel combinations of catalyst structures and components should be emphasized on mass of catalytic active site, adsorption of reactants and desorption of products in the catalytic process.

Compared to the sheets/film on the current collector, the nanotube arrays are superior in larger surface area, more available active sites, faster transport kinetics, and more defects involved in catalytic reaction thanks to spaces among the tubes [19, 20]. Yet, the tube array becomes an attractive morphology to lower the driving potential and promote the efficiency of water splitting. For example, Li's group used ZnO in the form of nanorod arrays as a template to fabricate FeOOH nanotube arrays in Ni foam for OER by electrodeposition [21]. However, ZnO must be removed by immersing in NaOH solution for a long time. Consequentially, the catalyst was

exposed to the risk of falling apart from Ni foam (NF), and deactivated due to replacement of active sites/defects in the catalyst body by ions from washing solution.

Herein, we design a novel route to synthesize FeNi hydroxides double-shell nanotube arrays (FeNi-HDNAs) on Ni foam by an in-situ reaction ($ZnO + M^{n+} + H_2O$ — $Zn^{2+} + M(OH)_n$, M= Fe or Ni). The process can be illustrated by Kirkendall effect, which is advanced in the following aspects. (i) ZnO rod arrays are removed by the in-situ reaction, simplifying preparation process and bolstering obtained structure. (ii) The in-situ reaction produces many pores and defects in arrays which can improve the OER electrocatalytic activity. (iii) The tube walls formed by nanoparticles are nanoscaled assemblies, which are endowed with the similar effective areas as super thin sheets. Finally, strong acid or alkali is not needed to remove ZnO rod templates, avoiding the loss of catalytically active sites on surface. Moreover, the combined spectroscopic determinations from the XPS and X-ray absorption near-edge structure (XANES) spectra show that electron migrations lead to a higher covalent state for Fe and more unoccupied Fe 3d states in the FeNi-HDNAs than the Fe hydroxides. Similar to design principles of perovskite oxides for ORR [22], more unoccupied Fe 3d states can serve better catalytic performance of the as-synthesized catalyst. As expected, the prepared FeNi-HDNAs with the above features exhibit lower overpotential (206mV at 10 mA cm^{-2}), excellent activity and durability for OER in alkaline electrolyte. DFT calculations reveal that the obtained structures lower the energy barrier of rate-determining step in OER. The overall water splitting from the FeNi-HDNAs provides a high current density of 10 mA cm^{-2} at a low cell voltage of

1.49 V and a durability of 100 h in alkaline solution.

2. Experimental section

2.1 Sample preparation

Ni foam (NF) was washed successively by sonication in acetone, absolute ethyl alcohol and deionized water. The dry NF was immersed into 0.5 mol/L $KMnO_4$ solution for surface activation. 20 mg $Zn(NO_3)_2 \cdot 6H_2O$ was dispersed into the mixed solution of 50 μL Nafion, 100μL isopropanol and 850 μL deionized water under stirring. 200 μL mixed Zn^{2+} solution was daubed on the surface of the activated NF, which was then dried in 60 °C oven. The $Zn(NO_3)_2$-covered NF was heated in the tubular furnace for 2h at 400 °C under N_2 to obtain ZnO seeds on the surface. Next, the ZnO rod arrays were grown in the autoclave with the mixed solution of HMTA and $Zn(NO_3)_2$ at 95 °C. Finally, the NF covered by ZnO rod arrays was washed several times by deionized water and dried for use.

The above ZnO-array covered NF (1 cm^2) was immersed into 0.005 mol/L $FeCl_3$ solutions for 2 min. Then it was transferred into 0.05 mol/L $NiCl_2$ solutions until no Zn^{2+} could be detected in the arrays. The product was washed several times by deionized water and ethanol, and finally dried in the oven for electrochemical test.

Pure $Fe(OH)_3$ and $Ni(OH)_2$ nanotube arrays on NF were prepared through similar protocols. They were obtained by extending the reaction time between ZnO rod arrays and $FeCl_3$ or $NiCl_2$ solutions until Zn^{2+} disappeared in the arrays.

2.2 Catalysts Characterization

Powder XRD data were acquired on a Bruker D8-Advance diffractometer with Cu Kα radiation (λ = 1.548 Å). The field emissions SEM (Hitachi s-4800) and TEM (TEM, FEI Tecnai G20, acceleration voltage 200 kW) were performed for the morphologies of the materials. The EDX and elemental mapping were also analyzed by FEI Tecnai G20. Specific surface areas and pore size distribution were investigated by N_2 physisorption at 77 K (model: BECKMAN SA3100 COULTER). XPS was performed in a Physical Electronics 5400 ESCA spectrometer with MgKa X-ray radiation at a power of 200 W for the elemental composition and valence state of the materials.

2.3 Electrochemical Measurements

The performance of as-prepared catalysts in OER was investigated in a three-electrode system in an alkaline electrolyte of 1.0 M KOH. A Pt wire and an Ag/AgCl electrode were used as the counter and reference electrodes respectively. All results were not compensated by iR-correction. The as-synthesized tube arrays on NF were used directly as working electrodes. RuO_2/NF working electrode was made by 5 μL mixed solution on NF, which typically consists of 4 mg of RuO_2 powder (Sigma-Aldrich), 1 mL of solvent (water and ethanol, 4:1, v/v) and 80 μL of Nafion solution. The electrolyte was bubbled by purging with argon for at least 30 min before measurement to remove oxygen dissolved in solution. Linear scan voltammetry (LSV) curves were recorded on the electrochemical workstation (Zahner Zennium) at a scan rate of 5 mV s^{-1}. Volt-time characteristic curves were performed on CHI 660. All potentials in this work were calibrated to RHE by equation $E_{(RHE)} = E_{(SCE)} + 0.241$

+0.059 pH, $E_{(OP)} = E_{(RHE)}$ - 1.23.

2.4 Method and Model of DFT Calculation

The surface structures of $Fe(OH)_3$, $Ni(OH)_2$ and FeNi hydroxides were first constructed, and the vacuum space along the z direction was set to 15 Å, which is enough to avoid interaction between the two neighboring images. The O, OH, OOH, O_2 groups were placed on surfaces of hydroxides. First-principles calculations in the framework of density functional theory, including structure and energy, were carried out based on the Cambridge Sequential Total Energy Package (CASTEP) [23]. The exchange–correlation functional under the generalized gradient approximation (GGA) [24] with norm-conserving pseudopotentials and Perdew–Burke–Ernzerhof functional was adopted to describe the electron–electron interaction [25]. An energy cutoff of 750 eV was used and a k-point sampling set of 5×5×1 was tested to be converged. A force tolerance of 0.01 eV $Å^{-1}$, energy tolerance of $5.0×10^{-7}$ eV per atom and maximum displacement of $5.0×10^{-4}$ Å were adopted. Each atom in the storage models is allowed to relax to the minimum in the enthalpy without any constraints. The water splitting can be divided into five steps [26]:

$$*+OH^- \rightarrow *OH \tag{1}$$

$$*OH + OH^- \rightarrow *O + H_2O \tag{2}$$

$$*O + OH^- \rightarrow *OOH \tag{3}$$

$$*OOH + OH^- \rightarrow *O_2 + H_2O \tag{4}$$

$$*O_2 \rightarrow * + O_2 (g) \tag{5}$$

Free energy change ΔG of the reaction was calculated as the difference between the

free energies of the initial and final states as shown below:

$$\Delta G = \Delta E + \Delta ZPE - T\Delta S$$

where E is the calculated energy by DFT, ZPE is the zero point energy, and S denotes the entropy.

2.5 Soft X-ray XANES analysis of Fe and Ni $L_{2,3}$ edges

The soft X-ray XANES spectra at the Fe and Ni $L_{2,3}$ absorption edges were recorded at room temperature in fluorescence mode at the plane grating monochromator (PGM) beam line [27] of the Physikalisch-Technische Bundesanstalt (PTB) at the BESSY II electron storage ring. This undulator beamline provides soft X-ray radiation of high spectral purity and high radiant power in the photon energy range of 78 eV to 1860 eV. Depending on the operational parameters, stray light contributions of about 0.5 % to 1 % have to be taken into account. The uncertainty of the energy scale of the PGM is in the 10-4 range. For the calibration of the PGM energy scale, typical resonance lines of Kr, Ar and Ne gases are used [28].

The experiments were carried out using an in-house developed ultrahigh vacuum chamber [29]. The samples were excited using an incident angle of 10° and the emitted Fe-L and Ni-L fluorescence radiation was detected using a calibrated silicon drift detector. For normalization purposes, the photon energy dependent incident flux of the beam line was measured beforehand using a calibrated photodiode.

3. Results and discussion

3.1 Morphology and structure of FeNi-HDNAs

The synthesis process of FeNi-HDNAs deposited on NF is illustrated in Fig. 1g. Firstly, ZnO nanorod arrays on NF are fabricated by seed growth according the previous work [30], as shown in Fig. S1. Secondly, the ZnO rod arrays are immersed into aqueous $FeCl_3$ solution and $Fe(OH)_3$ tube arrays are obtained facilely according to the reaction: $3ZnO + 2FeCl_3 + 3H_2O \rightarrow 2Fe(OH)_3 + 3ZnCl_2$ [31]. The formation of yolk-shell structure is a typical Kirkendall effect process where the outward diffusion of the inside Zn^{2+} ($J_{out(Zn)}$) is significantly faster than the inward diffusion of the outside Fe^{3+}($J_{in(Fe)}$). SEM images show the surface of rods becomes rougher while many nanoparticles turn out on them (Fig. S2a, b). It is revealed in TEM images that within the present yolk-shell structure, the inside nanorod has numerous defects and the outside shell is composed of many nanoparticles of ~5 nm diameter (Fig. S2c). The interplanar spacings of 0.52 and 0.27 nm from the inside rod and outside particles respectively match well with the [0001] plane of ZnO and the (220) plane of $Fe(OH)_3$. The energy–dispersive x-ray spectroscopy (EDX) elemental mapping from TEM show that Zn element stays totally inside of the rods and the Fe element locates at the outside of the shell. This further proves the rods are ZnO and the nanoparticles are $Fe(OH)_3$ (as shown in Fig. S2c). The ZnO rods can transform to $Fe(OH)_3$ tube completely in longer reaction time. However, the remained ZnO is important to bond the $Ni(OH)_2$ onto the $Fe(OH)_3$ tube arrays. The characteristic XRD patterns (JCPDS 74-2075) prove that the $Ni(OH)_2$ was successfully deposited onto arrays. More importantly, EDX analysis denotes the vanishing of ZnO in the arrays (Fig. S3), indicating complete reactions. The morphology of as-prepared FeNi-HDNAs is shown

in Fig. 1. The arrays still keep the uniform structures. The TEM images display the tubes are double shells with a thickness of ~20 nm. The different lattice planes of (220) $Fe(OH)_3$ and (011) $Ni(OH)_2$ are found in the inside and outside shell respectively. The SAED patterns are indexed to (213), (220) from $Fe(OH)_3$ and (111) (011) from $Ni(OH)_2$. The EDS elemental mapping identifies the $Ni(OH)_2$ resides at outside of the shell and $Fe(OH)_3$ inside, as given by the density distributions within the Fig. 1c.
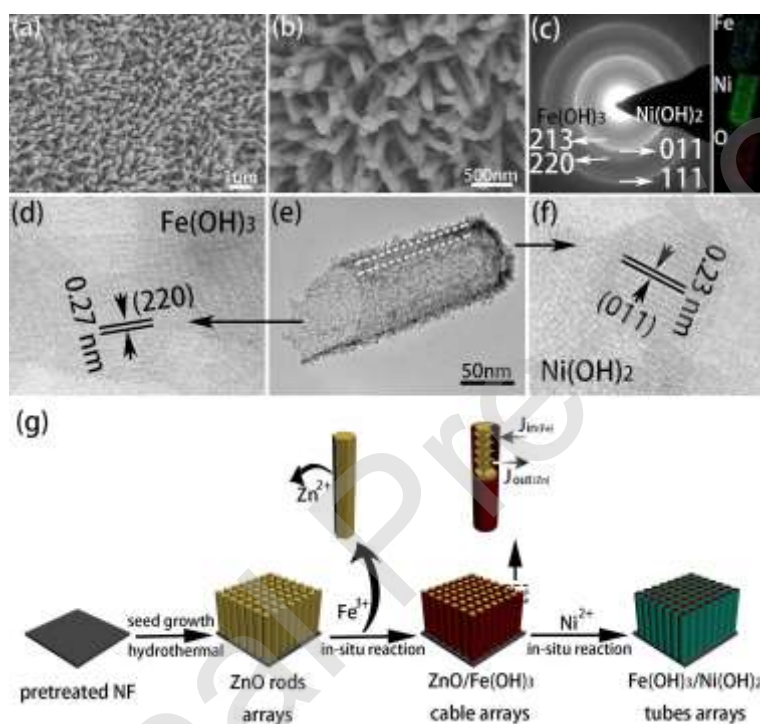

Fig. 1. (a), (b) SEM images, (c) SEAD pattern and EDS mapping, (d)-(f) TEM and HRTEM images of the as-prepared FeNi-HDNAs, (g) The illustration of the nanotube arrays on Ni foam by in-situ and Kirkendall process.

3.2 Electrochemical performances for OER of FeNi-HDNAs

To evaluate the electrocatalytic performance of the products toward OER, the obtained tube arrays were directly used as working electrodes. The electrochemical tests were performed in a typical three-electrode system with an electrolyte of O_2-saturated 1.0 M KOH aqueous solution and a scan rate of 5mV/s. Pt wire and the

calibrated Ag/AgCl were used as the counter and reference electrode. All electrochemical experiments were executed in room temperature and all results were converted as reversible hydrogen electrode (RHE). The linear sweep voltammetry (LSV) curves are presented in Fig. 2a. For comparison, the as-prepared FeNi-HDNAs, blank Ni foam (NF) and RuO_2/NF were investigated under same test conditions. The RuO_2 was coated on NF (RuO_2/NF) as given by the detailed method in the Supporting Information. The polarization curves of all catalysts are with iR correction. From Fig. 2c, it is clearly that FeNi-HDNAs have extreme overpotential (206 mV) at 10 mA cm^{-2}, which is substantially lower than that of RuO_2/NF (302 mV). Compared to results from previous works (Table S1), the overpotential is very low, which shows the in-situ and Kirkendall process is effective though it is very simple and convenient. Similar results are also seen at the higher current density where the FeNi-HD NAs electrodes require smaller overpotential of 274 mV compared to RuO_2/NF (366 mV) to achieve 50 mA cm^{-2}. Even though the current density is driven to 100 mA cm^{-2}, the overpotential applied on FeNi-HDNAs electrodes severally increase to 300 mV, still lower than that of RuO_2/NF (411 mV). The Tafel slopes are evaluated for catalytic reaction rates, as shown in Fig. 2b. It is obvious that the FeNi-HDNAs in-situ grown on NF have a smaller value (91.66 mV dec^{-1}) than commercial NF (138.24 mV dec^{-1}) and RuO_2/NF (109.92 mV dec^{-1}). This indicates that the as-prepared electrocatalysts favor the OER kinetics. The electrode stability is also one of the most important indexes in the electrocatalytic reaction. Fig. 2d shows chronopotentiometry curves (v-t) of FeNi-HDNAs in 1.0 M KOH aqueous solution. They exhibit a negligible rise

of applied overpotential in 10 h catalytic reaction at 10 mA cm^{-2}, 50 mA cm^{-2} and 100

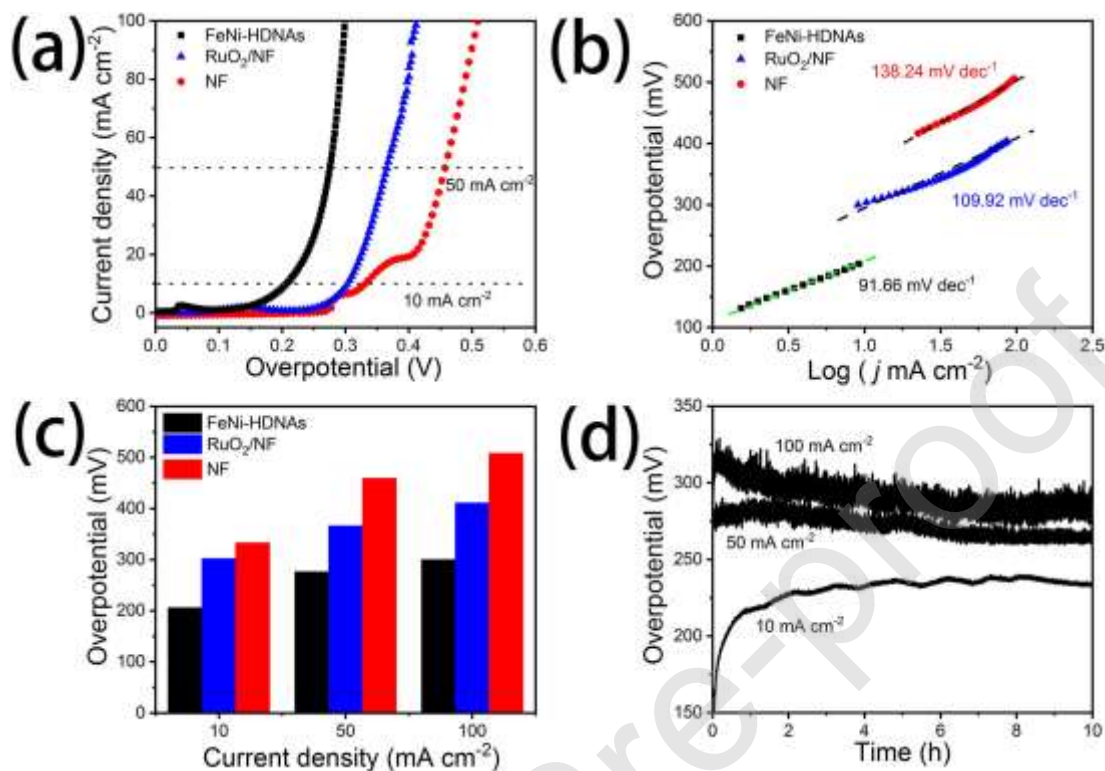mA cm^{-2}. The FeNi-HDNAs own long-term durability.

Fig. 2. (a) LSV curves and (b) Tafel slopes of the as-prepared FeNi-HDNAs in 1.0 M KOH at sweeping rate of 5mV/s. (c) The comparing column of overpotential and (d) v-t curves of FeNi-HDNAs at 10 mA cm^{-2}, 50 mA cm^{-2} and 100 mA cm^{-2}.

3.3 Morphology and structure of Fe(OH)₃ and Ni(OH)₂ tube arrays

For comparison purpose, the pure Fe(OH)$_3$ and Ni(OH)$_2$ tube arrays on NF were

prepared as electrodes for OER following the same synthesis as the FeNi-HDNAs.

The SEM images show Fe(OH)$_3$ tube arrays are composed of many uniform

nanotubes of ~100 nm diameter and rough surface (Fig. 3a, b). The TEM images in

Fig. 3c, d reveal that the tubes are formed by numerous nanoparticles with a size of ~5

nm and the wall thickness of tube is about 10 nm. Moreover, these porous tubes

possibly provide more channels to electrolyte in eletrocatalytic process. The HR-TEM

images show the interplanar spacing of nanoparticles is 0.27 nm (Fig. 3e, f), consistent with the $Fe(OH)_3$ (220) plane. The Zn element is not detected in EDS (Fig. S4), which indicates that ZnO completely reacted with $FeCl_3$.

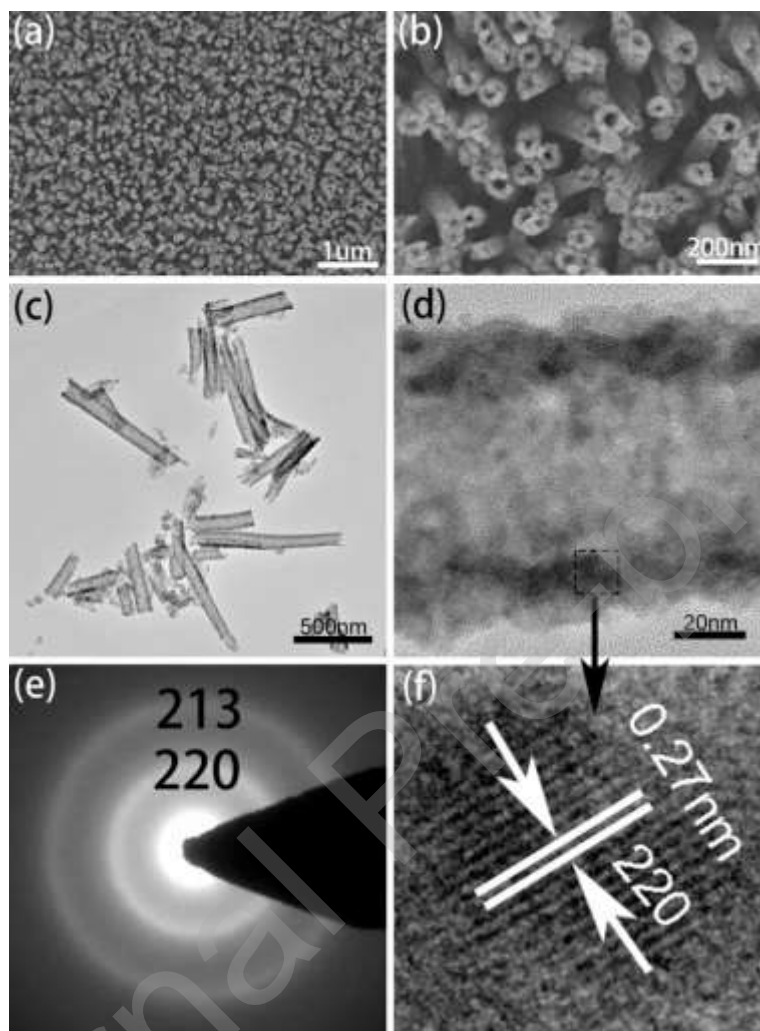**Fig. 3. (**a), (b) SEM images, (c), (d) TEM images, (e) SEAD pattern, (f) HRTEM of the as-prepared $Fe(OH)_3$ tube arrays.

It is well known that reaction between ZnO and $NiCl_2$ is more difficult than that between ZnO and $FeCl_3$ due to larger solubility production constant of $Ni(OH)_2$ (Ksp $= 2.0 \times 10^{-15}$) than $Fe(OH)_3$ (Ksp $= 4.0 \times 10^{-38}$). Longer reaction time and higher metal ion concentration are needed to prepare the $Ni(OH)_2$ tube arrays. We do not find the remained Zn element in the final arrays from EDX pattern, as shown in Fig. S5. The

final product is identified as Ni(OH)$_2$ nanotubes as given by the XRD patterns (JCPDS 74-2075) (Fig. S6). The SEM images display that the arrays remain intact though the rods are stuck together (Fig. 4a, b). It is obviously that the tubes have wide channels with a diameter of ~200 nm and narrow nanoshells of several tens of nanometer by TEM. Interestingly, the shell is covered by thinner sheets consisted of nanoparticles actually (Fig. 4c). Fig. 4d figures out that the interplanar spacing of 0.26 nm is indexed to the Ni(OH)$_2$ (011) plane.
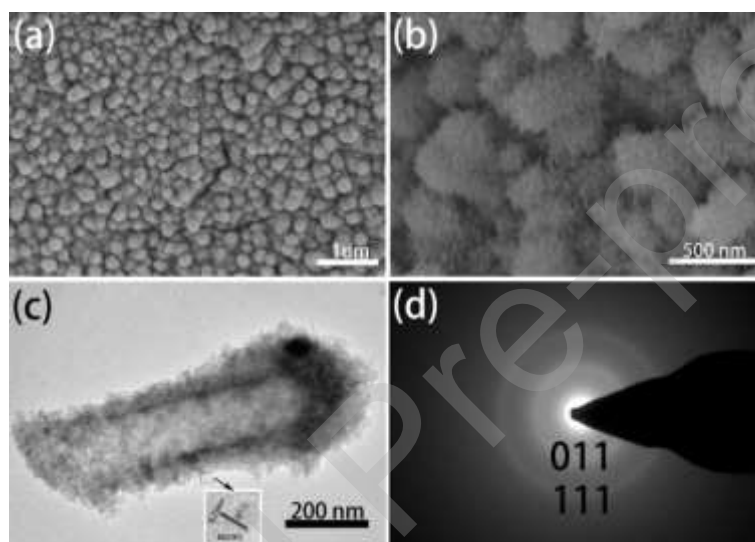

Fig. 4. (a) and (b) SEM images, (c) TEM images (the insert is HR-TEM image), (d) SEAD pattern, the as-prepared Ni(OH)$_2$ tubes arrays.

3.4 Electrochemical performances for OER of Fe(OH)$_3$ and Ni(OH)$_2$ tube arrays

The same electrochemical system was employed to evaluate the catalytic performance in OER of the electrodes made directly of Fe(OH)$_3$ and Ni(OH)$_2$ tube arrays on NF. The Fe(OH)$_3$ tube arrays possess lower overpotential (289 mV, 337 mV and 373mv) at 10 mA cm^{-2}, 50 mA cm^{-2} and 100 mA cm^{-2} shown in the LSV curves and the comparing column respectively (Fig. 5a, c). The catalytic activity is superior to that of RuO$_2$/NF. However, Ni(OH)$_2$ tube arrays have a peculiar phenomenon in

LSV curve. Its overpotential at different current density (Table 1) in OER catalysis is higher than that of RuO_2/NF, but lower than Ni foam and ZnO/NF. It is explained that Fe was not doped into $Ni(OH)_2$ tube arrays for the improved performance of OER. However, the Tafel slopes display that $Fe(OH)_3$ and $Ni(OH)_2$ electrodes made of tube arrays can speed up the reaction of water splitting because they have small value of 83.71 mV dec^{-1} and 90.74 mV dec^{-1} respectively (Fig. 5b). In the v-t curve (Fig. 5d), $Fe(OH)_3$ and $Ni(OH)_2$ tube arrays in-situ grown on NF have good stability in 1.0 M KOH at the steady current 10 mA cm^{-2} , 50 mA cm^{-2} and 100 mA cm^{-2}.
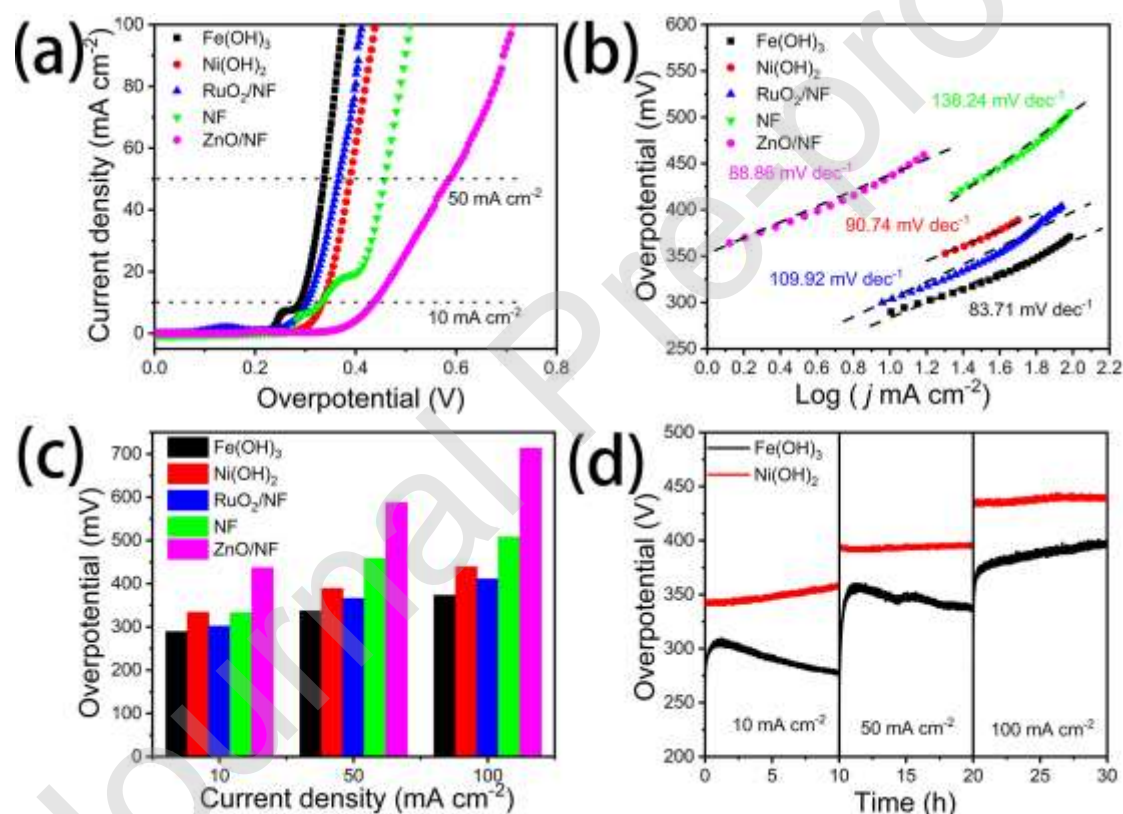

Fig. 5. (a) LSV curves and (b) Tafel slopes, (c) The comparing column of overpotential of the different electrodes and (d) v-t curves of $Fe(OH)_3$ and $Ni(OH)_2$ tube arrays at 10mA cm^{-2}, 50 mA cm^{-2} and 100 mA cm^{-2}.

We also compared the overpotentials and Tafel slopes in OER catalysis of the as-prepared eletrocatalysts, RuO_2/NF, and NF, which are shown in Table 1. It is found

that the as-synthesized arrays are superior to powder RuO_2 on NF. Firstly, the in-situ growth on the conductive Ni foam can improve the efficiency of electron collector in electrochemical reaction and reduce the interfacial barrier of electron transfer between the catalysts and electron collector. Secondly and more importantly, the porous and tube-like structures have bigger surface areas because the arrays avoid the aggregation of catalyst nanoparticles, which can absorb the reactant more easily than the powder catalysts. Besides, more catalytically active sites are exposed to reduce energy barrier of the catalytic reaction and promote its occurrence. Finally, the in-situ growth strengthens catalyst attachment to the substrate in the catalytic process compared to the powder catalysts on the glassy carbon electrode. This is beneficial to extend the working life of electrodes. Moreover, to further explain the intrinsic performance of the different electrocatalysts for OER, the current density is normalized by BET surface area of catalysts in order to exclude the influence of particle size on the intrinsic activity [32]. It is found obviously that the as-prepared electrocatalysts still exhibit the superior property (Fig. S8, 9).

3.5 Mechanism analysis

The electrocatalytic performance of FeNi-HDNAs is clearly superior to the Fe(OH)$_3$ and Ni(OH)$_2$ counterparts. X-Ray Photoelectron Spectroscopy (XPS) is carried out to investigate the surface states of the as-prepared tube arrays. Fig. S10 shows XPS survey spectra of FeNi-HDNAs, demonstrating the coexistence of Ni, Fe and O. This again confirms that Ni(OH)$_2$ was successfully prepared onto the array and is consistent with the XRD and EDS results.
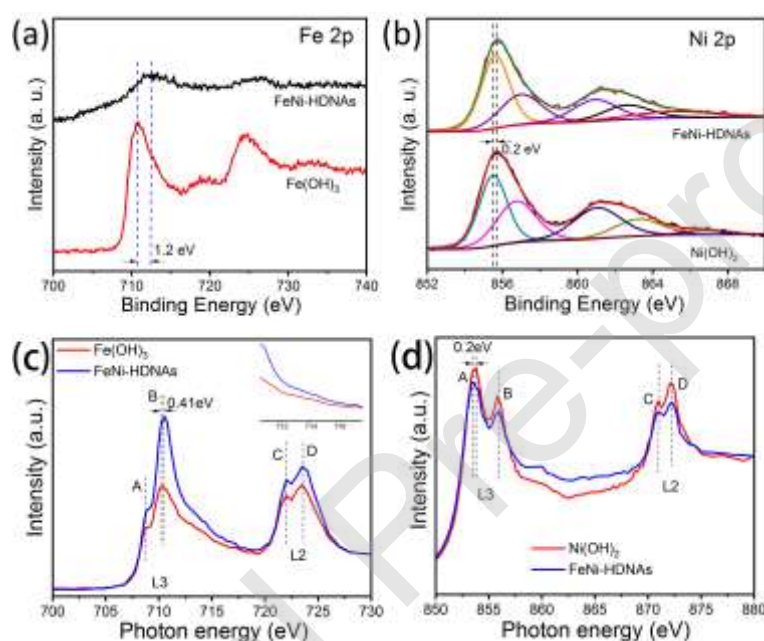

Fig. 6. XPS spectra of (a) Fe 2p and b) Ni 2p of the as-synthesized FeNi-HDNAs; (c) Fe and (d) Ni L$_{2, 3}$-edge XANES spectra of FeNi-HDNAs and the counterparts.

The specific oxidations states of Fe and Ni are analyzed in the high-resolution spectra (Fig. 6). Interestingly, it is exhibited clearly that the binding energy of Fe 2p in composite tubes shows a positive shift of 1.2 eV compared to the pure phase (Fig. 6a). However, the chemical shift is rather small for Ni 2p. After further peak fitting analysis of Ni 2p signal, a slight negative shift (0.2 eV) is found at Ni 2p$_{3/2}$ peak (Fig. 6b). The huge difference of their energy shifts is because the Ni content is much more than Fe on the surface of composite tubes. The above results indicate there is an

alteration of electronic structure contributing to interaction between Fe and Ni. It can enhance catalytic activity in OER because of facile electron transfer [33].

Soft X-ray absorption spectroscopy is employed to investigate interactions between Fe and Ni atoms in FeNi-HDNAs. Fig. 6c, d depict the $L_{2,3}$-edge X-ray absorption near-edge structure (XANES) spectra of Fe and Ni of the FeNi-HDNAs and Fe/Ni counterparts. The 3d valence states are detected by excitation of 2p core electron into empty 3d orbitals [18]. It is clearly found that Fe has a positive energy shift (0.41 eV, peak B in Fig. 6c) in FeNi-HDNAs compare to the pure $Fe(OH)_3$, while Ni shows a negative shift (~0.2 eV, peak B in Fig. 6d). The chemical shift trend is consistent with the results of XPS. Detailed orbital analysis is carried out through the XANES structures. In Fig. 6c, peaks A and C denote photoexcitation from 2p orbitals to the 3d t_{2g} unoccupied orbitals and peak B and D the e_g orbitals in the octahedral crystal field [33]. The peaks A and B are characteristic features of Fe +2 and +3 valence state. The intensity of peak B of FeNi-HDNAs is stronger than that of $Fe(OH)_3$. The intensity ratios of peak B and A of the two samples are 2.1 and 1.6 respectively, which indicates more unoccupied Fe 3d states in the FeNi-HDNAs. Moreover, the intensity of resonance center also explains the valence state of Fe according to Wang's report [33]. As shown in Fig. 6c, the resonance intensities of Fe $L_{2,3}$-edge spectra from FeNi-HDNAs are higher than these in the pure phase, which shows that Fe has higher oxidation state again. The higher valence state indeed improves largely the eletrocatalytic activity for OER because it lowers the adsorption free energy of intermediate on the Fe sites [9]. Fig. 6d is the $L_{2,3}$-edge XANES spectra of Ni for

investigation of excitation electron from 2p to 3d. Interestingly, the intensities of higher oxidation states (peak B) are strong in both samples. We presume that the in-situ reaction lead to many defects and holes in the structure. But in contrast to the results of Fe, intensity ratio of peak B and A of FeNi-HDNAs decreased compared to $Ni(OH)_2$. This is attributed to more electrons present in 3d orbital of Ni which reduces the Ni oxidation state. Comparing the XANES structures between Fe and Ni, electrons migrate from Fe d orbital to the Ni d orbital, leaving more oxidization for Fe but reduction to the Ni [35]. Thus, Fe with higher oxidation state improves the electrocatalytic activity of FeNi-HDNAs and the interaction of Fe and Ni benefits electrocatalytic performance for OER. Besides, high density of t_{2g} unoccupied states attributes to Fe 3d electron delocalization in mixed valence of FeNi hydroxides, which enhances electron transfer in OER electrocatalysis because of Fe d-orbital overlap under bias voltages [36].

It is well known that OER is considered as the following traditional process involving proton–electron transfer in alkaline media [37], which is shown in Scheme S1. Firstly, OH gets close to the metal active site and loses an electron; the active site adsorbs OH (M-OH). Secondly, a proton and electron transfer and M-O forms by another OH approaches M-OH. Thirdly, M-O interact with OH to form M-OOH as an electron loses. Subsequently, O-O forms at the active site when OH reacts M-OOH with H_2O production and an electron transfer. Finally, O-O desorbs off catalyst surface for O_2 (g); while the catalyst goes to the next cycle.
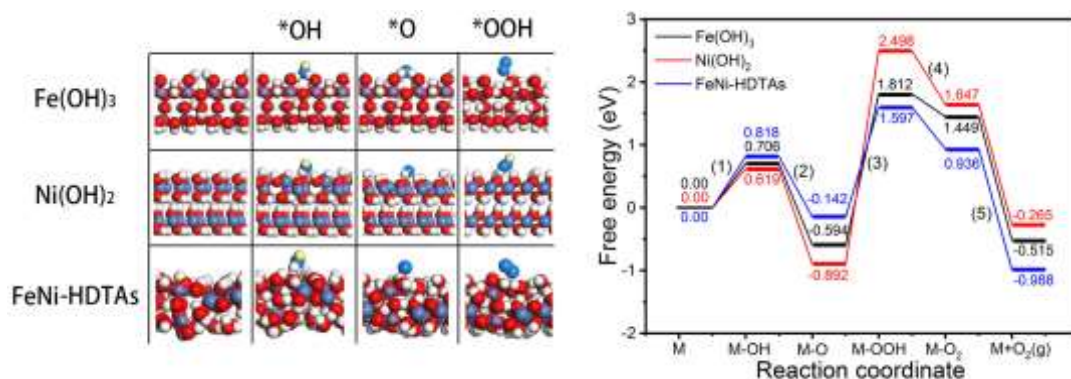
Fig. 7. Adsorption geometries (left) and free energy (right) of the catalysts and the intermediates.

The DFT calculation is further employed to explicate the mechanisms of superior OER performances of the as-prepared electrocatalysts. In the catalyst structures (Fig. 7a), it is found that *OOH is absorbed by direct single hydrogen bond to the Fe and Ni catalysts, but it is stabilized via indirect bond to Fe-Ni surface. The free energy changes of intermediates (M-OH, M-O, M-OOH, M-O_2) and products (M+O_2) are shown in Fig. 7b. Ni(OH)$_2$ based catalysts have highest free energy of intermediates expect of M-OH, which indicates the binding between Ni(OH)$_2$ surface and the intermediates is the strongest while its adsorption of *OH is the weakest. ΔG of each fundamental reaction of OER in the different catalysts is listed in Table 2. It displays that transformation *O to*OOH is rate-determining step because$\Delta G_3 >> \Delta G_1$, ΔG_2, ΔG_4, ΔG_5. Comparing three catalysts, it is found obviously that $\Delta G_{3\ (FeNi-HDNAs)} < \Delta G_{3\ (Fe(OH)3)} < \Delta G_{3\ (Ni(OH)2)}$, which hints that the formation *OOH from *O on the surface of FeNi-HDNAs catalysts is easier than Fe(OH)$_3$ and Ni(OH)$_2$. In another words, FeNi-HDNAs is favorable to oxidize water to oxygen attributing that it lowers the energy barrier of rate-determining step in OER.

3.6 Electrochemical performance for HER of the as-prepared tube arrays

It is well-known that improvement of hydrogen evolution reaction (HER) performance is challenging for the electrocatalysts in the alkaline solution. Certainly, it is also curious whether the as-synthesized nanotube arrays promote the electrocatalytic activity for HER and overall water splitting. The HER electrocatalytic activities of three samples were evaluated by LSV curves in 1.0 M KOH solution similarly and the commercial Pt/C was for comparison, which is displayed in Fig. 8a. At a current density of 10 mA cm^{-2}, the electrodes based FeNi-HDNAs, Fe(OH)$_3$ and Ni(OH)$_2$ nanotube arrays show the overpotential of 141 mV, 153 mV and 179 mV respectively (Fig. S11). The overpotentials still have some gaps between the as-synthesized nanotube arrays and commercial Pt/C on NF (43 mV), but they take a step compare to the bulk Fe(OH)$_3$, Ni(OH)$_2$ and FeNi double hydroxides on NF. It indicates the as-synthesized electrocatalysts shaped tube arrays have unique advantages. The Tafel plots of the different electrocatalysts are shown in Fig. 8b. FeNi-HDNAs have the lowest value (184 mV dec^{-1}) in the as-synthesized tube arrays except for commercial Pt/C, which indicates FeNi-HDNAs is most favorable for HER kinetics in alkaline media too.
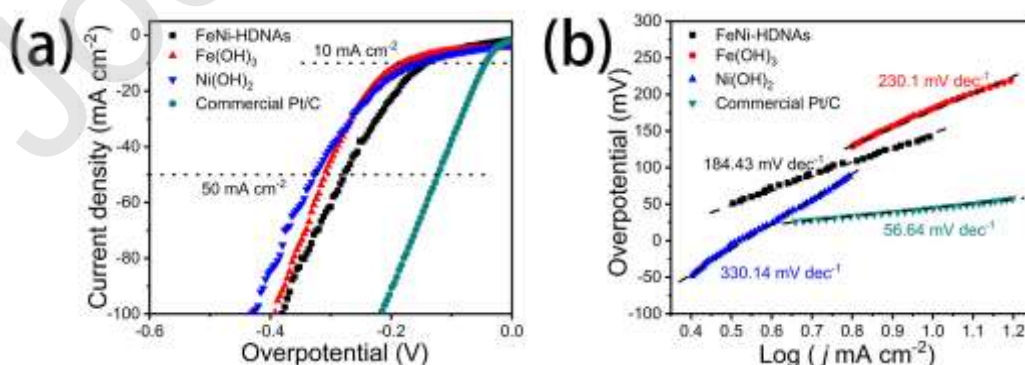
Fig. 8. (a) LSV curves of overpotential and (b) Tafel slopes for HER of FeNi-HDNAs, Fe(OH)$_3$ and Ni(OH)$_2$ tube arrays in 1.0 M KOH.

3.7 Electrocatalytic performance for overall water splitting of FeNi-HDNAs

The above electrocatalytic results indicate that FeNi-HDNAs can directly work as the anode and cathode for water splitting because they exhibit excellent activity and durability in strong alkali solution (1.0 M KOH), as shown in Fig. 9a. FeNi-HDNAs were applied with a low cell voltage of 1.49 V as current density is driven to 10 mA cm^{-2} (Fig. 9b), which is lower than values in most of previous works (Table S1). As shown in the video (Supporting information), large amount of O$_2$ and H$_2$ bubbles emerged obviously on the anode and cathode. Additionally, the LSV and v-t curves display FeNi-HDNAs only emerge obvious cell voltage augment 6 mV and 7 mV at a constant current density of 10 mA cm^{-2} and 50 mA cm^{-2} during 100 h water electrolysis in alkali solution, respectively (Fig. 9c, d). The results prove that the as-synthesized FeNi-HDNAs are very promising candidate for electrocatalytic overall water splitting.
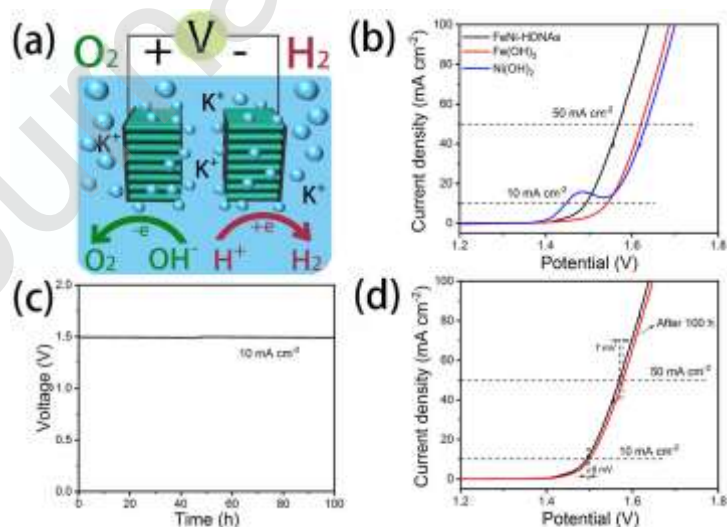

Fig. 9. (a) Scheme of water splitted by as-prepared electrodes; (b) LSV curves of FeNi-HDNAs‖FeNi-HDNAs, Fe(OH)$_3$ tube arrays‖Fe(OH)$_3$ tube arrays, Ni(OH)$_2$ tube

arrays‖Ni(OH)$_2$ tube arrays for water splitting in 1.0 M KOH; (c) v-t curve of FeNi-HDNAs water splitting at 10 mA cm^{-2}; (d) LSV curves of FeNi-HDNAs before and after 100h durability test at 10 mA cm^{-2}.

4. Conclusions

In conclusion, the electrocatalysts for OER based Fe(OH)$_3$, Ni(OH)$_2$ and FeNi-HDNAs on NF were fabricated by an in-situ reaction and Kirkendall effect. They exhibited superior electrocatalytic performance of OER compared to RuO$_2$ on NF. The FeNi-HDNAs own an especially extremely low overpotential (206 mV) at 10 mA cm^{-2}. XPS and XANES show that the superior performance is attributed to more unoccupied Fe 3d states in the FeNi-HDNAs. The as-prepared electrodes showed a long-term durability in alkaline electrolyte because they reduced the risk of falling off from the substrate thanks to the in-situ growth on the metal substrate. Compared to the powder electrocatalysts, the as-synthesized tube arrays on NF are advanced in higher specific surface area, greater number of active sites and better stability. It is revealed by DFT calculation that FeNi hydroxides served the largest reduction of ΔG of rate-determining step for OER. In the overall water splitting, FeNi-HDNAs drive the current density of 10 mA cm^{-2} with a low cell voltage of 1.49 V and display excellent stability over 100 h measurement. The present work offers a novel and highly efficient strategy to reach practical functionalities in electrocatalysts for OER.

Appendix A. Supporting information

Supplementary data associated with this article can be found in the online version at doi:*****************

References

[1] L. Han, S.J. Dong, E.K. Wang, Adv. Mater. 28 (2016) 9266-9291.

[2] Y. Matsumoto, E. Sato, Mater. Chem. Phys. 14 (1986) 397−426.

[3] S. Trasatti, O.A. Petrii, J. Electroanal. Chem. 327 (1992) 353−376.

[4] S. Trasatti, J. Electroanal. Chem. 111 (1980) 125−131.

[5] S. Trasatti, O.A. Petrii, Pure Appl. Chem. 63 (1991) 711−734.

[6] J. Rossmeisl, K. Dimitrievski, P. Siegbahn, J.K. Nørskov, J. Phys. Chem. C 111 (2007) 18821−18823.

[7] J. Rossmeisl, Z.W. Qu, H. Zhu, G.J. Kroes, J.K. Nørskov, J. Electroanal. Chem. 607 (2007) 83−89.

[8] M.W. Louie, A.T. Bell, J. Am. Chem. Soc. 135 (2013) 12329−12337.

[9] D. Friebel, M.W. Louie, M. Bajdich, K.E. Sanwald, Y. Cai, A.M. Wise, M.J. Cheng, D. Sokaras, T.C. Weng, R. Alonso-Mori, R.C. Davis, J.R. Bargar, J.K. Nørskov, A. Nilsson, A.T. Bell, J. Am. Chem. Soc. 137 (2015) 1305−1313.

[10] L.L. Feng, G. Yu, Y. Wu, G.D. Li, H. Li, Y. Sun, T. Asefa, W. Chen, X. Zou, J. Am. Chem. Soc. 137 (2015) 14023−14026.

[11] C.G. Hu, L.M. Dai, Adv. Mater. 29 (2017) 1604942.

[12] D.A. Corrigan, J. Electrochem. Soc. 134 (1987) 377−384.

[13] X. Long, S. Xiao, Z. Wang, X. Zheng, S. Yang, Chem. Commun. 51 (2015) 1120−1123.

[14] M. Gong, Y. Li, H. Wang, Y. Liang, J.Z. Wu, J. Zhou, J. Wang, T. Regier, F. Wei,

H. Dai, J. Am. Chem. Soc. 135 (2013) 8452−8455.

[15] X. Long, J. Li, S. Xiao, K. Yan, Z. Wang, H. Chen, S. Yang, Angew. Chem. Int. Ed. 53 (2014) 7584−7588.

[16] D. Tang, J. Liu, X. Wu, R. Liu, X. Han, Y. Han, H. Huang, Y. Liu, Z. Kang, ACS Appl. Mater. Interfaces 6 (2014) 7918−7925.

[17] W. Zhang, Y.Z. Wu, J. Qi, M.X. Chen, R. Cao, Adv. Energy Mater. 8 (2017) 1602547.

[18] H.Y. Li, S.M. Chen, Y. Zhang, Q.H. Zhang, X.F. Jia, Q. Zhang, L. Gu, X.M. Sun, L. Song, X. Wang, Nat. Commun. 9 (2018) 2452.

[19] G. Prieto, H. Tüysüz, N. Duyckaerts, J. Knossalla, G.H. Wang, F. Schüth, Chem. Rev. 116 (2016) 14056−14119.

[20] J.F. Xie, X.D. Zhang, H. Zhang, J.J. Zhang, S. Li, R.X. Wang, B.C. Pan, Y. Xie, Adv. Mater. 29 (2017) 1604765.

[21] J.X. Feng , S.H. Ye , H. Xu , Y.X. Tong , G.R. Li, Adv. Mater. 28 (2016) 4698−4703.

[22] J. Suntivich, H.A. Gasteiger, N. Yabuuchi, H. Nakanishi, J. B. Goodenough, Y, Shao-Horn, Nat. Chem. 3 (2011) 546−550.

[23] Payne, J. Phys.: Condens. Matter. 14 (2002) 2717−2744.

[24] J.P. Perdew, K. Burke, M. Ernzerhof, Phys. Rev. Lett. 77 (1996) 3865−3868.

[25] D.R. Hamann, M. Schl˙uter, C. Chiang, *Phys. Rev. Lett*. 43 (1979), 1494−1497.

[26] D. Voiry, H. Yamaguchi; J. Li; R. Silva; D.C.B. Alves; T. Fujita; M.W. Chen; T. Asefa; V. Shenoy; G. Eda; M. Chhowalla, Nat. Mater. 12 (2013) 850−855.

[27] F. Senf, U. Flechsig; F. Eggenstein, W. Gudat, R. Klein, H. Rabus, G. Ulm, J. Synchrotron Rad. 5 (1998) 780−782.

[28] F.Scholze, B. Beckhoff, G. Brandt, F. Fliegauf, A. Gottwald, R. Klein, B. Meyer, D. Rost, U. Schwarz, R. Thornagel, J. Tümmler, K. Vogel, J. Weser, G. Ulm, Proc. SPIE 4344 (2001) 402.

[29] J. Lubeck, B. Beckhoff, R. Fliegauf, I. Holfelder, P. Hönicke, M. Müller, B. Pollakowski, F. Reinhardt, J. Weser, Rev. Sci. Instrum. 84 (2013) 045106.

[30] P. Yang, X. Xiao, Y. Li, Y. Ding, P. Qiang, X. Tan, W. Mai, Z. Lin, W. Wu, T. Li, H. Jin, P. Liu, J. Zhou, C.P. Wong, Z. Wang, ACS Nano 7 (2013) 2617−2626.

[31] Q. Wang, B.Y. Geng, S.S. Wang, Y.X. Ye, B. Tao, Chem. Commun. 46 (2010) 1899−1901.

[32] S.N. Sun, H.Y. Li, Z. J. Xu, Joule 2 (2018) 1–4.

[33] V.R. Stamenkovic, B.S. Mun, M. Arenz, K.J.J. Mayrhofer, C. A. Lucas, G. Wang, P.N. Ross, N.M. Markovic, Nat. Mater. 6 (2007) 241–247.

[34] D.N. Wang, J.G. Zhou, Y.F. Hu, J.L. Yang, N. Han, Y.G. Li, T.K. Sham, J. Phys. Chem. C 119 (2015) 19573−19583.

[35] J. Zhou, P.N. Duchesne, Y. Hu, J. Wang, P. Zhang, Y. Li, T. Regier, H. Dai, Phys. Chem. Chem. Phys. 16 (2014) 15787–15791.

[36] S.C. Chen, Z.X. Kang, X.D. Zhang, J.F. Xie, H. Wang, W. Shao, X.S. Zheng, W.S. Yan, B.C. Pan, Y. Xie, ACS Cent. Sci. 3 (2017) 1221−1227.

[37] A. Grimaud, O. Diaz-Morales, B. Han, W.T. Hong, Y.L. Lee, L. Giordano, K.A. Stoerzinger, M.T.M. Koper, Y. Shao-Horn, Nat. Chem. 9 (2017) 457−465.

Table 1. The comparison of the electrocatalytic OER activity of the different samples for OER in 1.0 M KOH.

Catalysts	Overpotential (mV) at			Tafel slopes
	10 mA cm^{-2}	50 mA cm^{-2}	100 mA cm^{-2}	(mV dec^{-1})
FeNi-HDNAs	206	274	300	91.66
Fe(OH)$_3$	289	337	373	83.71
Ni(OH)$_2$	334	389	439	90.74
RuO$_2$/NF	302	366	411	109.92
NF	333	459	508	138.24
ZnO/NF	437	587	713	88.86

Table 2. ΔG of each fundamental reaction of OER in the different catalysts.

Catalysts	Free energy (eV)					ΔG (eV)				
	M-OH	M-O	M-OOH	M-O$_2$	M+O$_2$(g)	ΔG_1	ΔG_2	ΔG_3	ΔG_4	ΔG_5
Ni(OH)$_2$	0.619	-0.892	2.498	1.647	-0.265	0.619	1.511	3.39	0.851	1.912
Fe(OH)$_3$	0.706	-0.594	1.812	1.449	0.515	0.706	1.3	2.406	0.363	1.964
FeNi-HDNAS	0.818	-0.142	1.597	0.936	-0.988	0.818	0.96	1.739	0.661	1.924